Proceedings of the ASME 2026 45th International Conference on Ocean, Offshore and Arctic Engineering
OMAE2026
June 7-12, 2026, Tokyo, Japan

OMAE2026-181891

NUMERICAL INVESTIGATION OF SUBMARINE-BRASH ICE INTERACTION BASED ON CFD-DEM COUPLING METHOD

Yongzhi Guo
Computational Marine Hydrodynamic Lab (CMHL), School of Ocean and Civil Engineering, Shanghai Jiao Tong University, Shanghai, China

Liushuai Cao
Computational Marine Hydrodynamic Lab (CMHL), School of Ocean and Civil Engineering, Shanghai Jiao Tong University, Shanghai, China

Decheng Wan*
Computational Marine Hydrodynamic Lab (CMHL), School of Ocean and Civil Engineering, Shanghai Jiao Tong University, Shanghai, China

ABSTRACT

With the continuous retreat of Arctic sea ice due to global warming, the navigability of Arctic shipping routes has significantly improved, leading to increasing operational demands for submarines in ice-covered waters. This study employs a CFD-DEM coupling approach to numerically investigate the interaction between a submarine and brash ice during near-surface navigation through a brash ice channel. Based on the STAR-CCM+ platform, the Discrete Element Method (DEM) is employed to simulate ice floe motion and inter ice collisions. Using the Joubert BB2 submarine as the research object, the effects of submergence depth, ice floe size, and forward speed on ice distribution patterns and ice loads are systematically analyzed. The results indicate that mean ice loads at shallow submergence h=0.3B are 2-3 times higher than those at greater depths, where h is the submergence depth and B is the submarine beam. Increasing ice floe radius leads to an order of magnitude increase in peak ice loads. Mean ice loads increase by approximately 6-7 times as speed rises from 5 kn to 8 kn, although the growth rate diminishes beyond a certain velocity threshold. The findings provide valuable references for submarine operational safety assessment and hull structural design in ice-infested waters.

Keywords: Submarine; Brash Ice; CFD-DEM Coupling; Ice Load; Numerical Simulation

1. INTRODUCTION

The Arctic region, serving as the shortest maritime route connecting Asia, Europe, and North America, holds unique and paramount strategic significance. Historically, year-round navigation through this region has been severely impeded by extensive ice coverage. Over the past five decades, Arctic sea ice extent has exhibited a persistent declining trend, substantially enhancing the navigability of Arctic waters and thereby amplifying the region's geostrategic importance.

Conventionally, submarines navigate beneath ice sheets to maintain stealth, leveraging the acoustic shielding properties of ice cover to evade detection. However, emergency situations or urgent operational requirements may necessitate breaching the ice canopy to surface. While direct impact with thick ice poses a significant risk of structural damage, the ongoing thinning and fragmentation of Arctic sea ice, in conjunction with advances in icebreaking capabilities, have considerably expanded the operational envelope for submarine activities in polar regions[1]. During surface or near-surface operations, drifting ice floes present potential hazards to submarine hulls. The interaction mechanisms between submarines and fragmented ice remain insufficiently understood, underscoring the imperative for systematic research in this domain.

Current research efforts have predominantly concentrated on ship-brash ice interaction, employing model-scale experiments and numerical simulations as the principal investigative methodologies. Through decades of development, a diverse array of numerical approaches has been established and implemented, notably including the Discrete Element Method (DEM), Peridynamics, and the Finite Element Method (FEM). Zou et al.[2] employed dynamic overset grid technology and the DFBI method to simulate the free-running motion of ships in pack ice areas. A coupled CFD-DEM numerical model was developed, and its effectiveness was validated through comparison with model test data. Xie et al.[3] used a coupled CFD-DEM approach to simulate ship navigation in brash ice channels, achieving less than 5% deviation from HSVA ice tank tests, and analyzed the effects of friction coefficient, ice thickness, ice shape, and ice concentration on resistance. Zhang et al.[4] investigated ship-brash ice interaction using a CFD-DEM approach, comparing three contact models with resistance errors within 5.5%, and identified ice shape as a critical factor affecting ice resistance. Huang et al. [5-6] developed an empirical equation for ice-floe resistance prediction based on extensive CFD-DEM simulations, incorporating ship geometry, speed, ice concentration, and floe dimensions, with its accuracy validated against multiple data sources. Wang et al.[7] used the finite element method to simulate bulk carrier navigation in brash ice fields, achieving ice resistance predictions within 15% deviation, and systematically analyzed the effects of speed and ice concentration on ice load characteristics. Ibrahim et al.[8] reviewed ice load problems for ships and offshore structures, summarizing ice-structure dynamic interactions, probabilistic ice load models, design regulations, and ship motion control schemes.

Submarines differ substantially from surface vessels in terms of structural configuration, driven by distinct design philosophies, operational environments, and mission profiles. Consequently, the direct application of ship-ice interaction findings to submarine scenarios is inherently limited. This underscores the engineering imperative and practical significance of investigating submarine-brash ice interaction in ice-covered waters.

2. NUMERICAL METHODS

2.1 Governing Equations

The software used in this study is STAR-CCM + 2302. In the simulation, the Navier-Stokes equation based on the Reynolds average (RANS) is used as the governing equation of fluid motion, and its expressions are as follows:

$$\frac{\partial \overline{u_i}}{\partial x_i} = 0 \tag{1}$$

$$\rho \frac{\partial \overline{u_i}}{\partial_t} + \rho \overline{u_j} \frac{\partial \overline{u_i}}{\partial x_j} = -\frac{\partial \overline{p}}{\partial x_i} + \mu \frac{\partial^2 \overline{u_i}}{\partial x_j \partial x_j} + \frac{\partial \left(-\rho \overline{u_i^{'} u_j^{'}} \right)}{\partial x_j} \tag{2}$$

In the above equation, $\overline{u_i}$ and $\overline{u_j}$ are the time mean of velocity pulsation, ρ is the fluid density, p is time mean pressure, and μ is the dynamic viscosity. In this study, the $k-\omega$ model proposed by Menter [9] is selected to make the above equation closed.

2.2 Basic theory of DEM

In the DEM framework, ice floes are discretized as composite assemblies comprising multiple elementary spherical particles, with inter-particle contact forces governed by a spring-dashpot model. As illustrated in Fig. 1, the contact force at the interaction point between adjacent ice elements is modeled using a spring-dashpot oscillator pair. The spring component characterizes the elastic repulsive force arising from particle collision, whereas the dashpot component captures the energy dissipation associated with inelastic contact behavior[10].

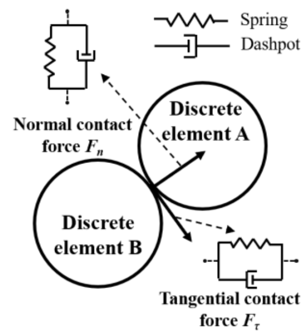

FIGURE 1. DISCRETE ELEMENT CONTACT FORCE MODEL

During submarine-ice-water interaction, ice floes experience coupled translational and rotational motions governed by the following equations:

$$m \frac{dv}{dt} = F_g + F_c + F_f \tag{3}$$

$$I \frac{d\omega}{dt} = M_c + M_f \tag{4}$$

where m denotes the mass of an individual ice floe and v is translational velocity. The forces acting on each ice element comprise gravitational force F_g, inter-body contact force F_c, and fluid-induced hydrodynamic force F_f. The rotational dynamics are characterized by the moment of inertia I and angular velocity ω, with M_c and M_f representing the torques arising from contact interactions and hydrodynamic loading, respectively.

The contact force F_c between two discrete elements is decomposed into normal and tangential components:

$$F_c = F_n + F_t \tag{5}$$

The normal and tangential contact forces are computed as:

$$F_n = K_n \delta_n + N_n \dot{\delta}_n \tag{6}$$

$$F_t = \min\left(K_t \delta_t + N_t \dot{\delta}_t, \mu_s \left| F_n \right| \right) \tag{7}$$

where K_n and K_t are the normal and tangential spring stiffnesses, respectively; δ_n and δ_t denote the normal and tangential overlaps; N_n and N_t represent the normal and tangential damping coefficients; and $\dot{\delta}_n$ and $\dot{\delta}_t$ are the relative velocities in the normal and tangential directions, respectively. The tangential force is limited by Coulomb's friction law, where μ_s is the static friction coefficient. The coupling between the fluid and brash ice is implemented via two-way interaction, wherein mass, momentum, and energy are exchanged between the Eulerian continuous phase and the Lagrangian discrete phase[11].

2.3 CFD-DEM coupling method

Currently, CFD-DEM coupling approaches are generally categorized into one-way and two-way coupling schemes. In two-way coupling, mutual interactions between the fluid phase and discrete ice floes are fully resolved, whereas one-way coupling solely accounts for the influence of hydrodynamic forces on ice floe motion, neglecting the reciprocal effect of ice on the flow field. Previous investigations have indicated that the discrepancy in ice resistance predictions between these two coupling schemes is marginal[11]. Given that one-way coupling offers substantial advantages in computational efficiency, this approach is employed in the present study.

3. COMPUTATIONAL SETUP

3.1 Geometry

The submarine model employed in this study is the Joubert BB2, a generic submarine geometry developed by the Defence Science and Technology (DST) Group [12-13]. The BB2 model incorporates simplified yet representative features of modern submarine configurations, including a streamlined hull, sail, stern control surfaces, and bow planes. Fig. 2 illustrates the geometric model of the submarine, and Tab. 1 summarizes the principal parameters of the submarine at a scale ratio of 1:18.348.

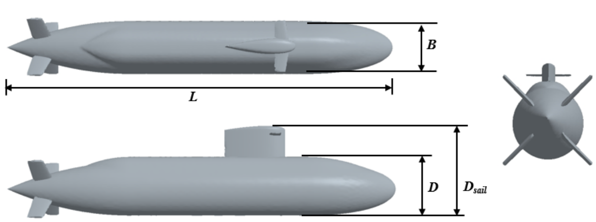

FIGURE 2. THE MODEL OF BB2 SUBMARINE

TABLE 1. MAIN PARAMETERS OF BB2 SUBMARINE

Description	Symbol	Model Scal (*m*)
Length	L	3.526
Beam	B	0.5232
Drought to deck	D	0.5777
Drought to sail	D_{sail}	0.8829

3.2 Computational Domain and Mesh

In the present simulations, the submarine remains stationary with a prescribed uniform inflow velocity. This approach is equivalent to a submarine advancing at constant speed and is computationally advantageous for mesh handling. As depicted in Fig. 3, the computational domain extends 7L, 6L, and 6L in the streamwise, transverse, and vertical directions, respectively, where L denotes the submarine length. The upstream boundary is specified as a velocity inlet, the downstream boundary is set as a pressure outlet, and all remaining boundaries are treated as no-slip walls.

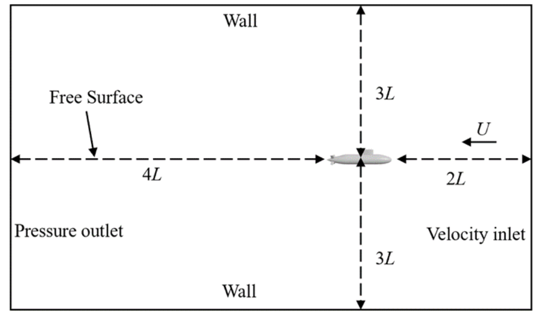

(a) Side view

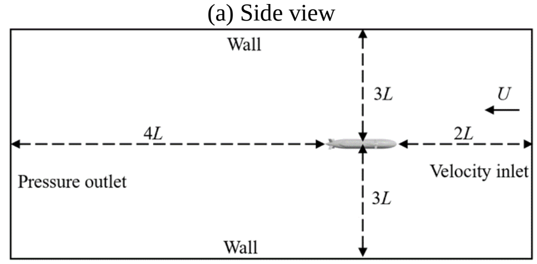

(b) Top view

FIGURE 3. COMPUTATIONAL DOMAIN

The computational mesh is generated using a trimmed cell mesher for the bulk domain, complemented by a prism layer mesher in the near-wall region surrounding the submarine hull to ensure adequate resolution of the boundary layer. Given that the present study focuses primarily on ice-induced loads on the submarine, local mesh refinement is implemented in the vicinity of the free surface and the hull surface. A mesh convergence analysis was conducted, yielding a final mesh comprising approximately 1.45 million cells. The local mesh distribution is presented in Fig. 4.

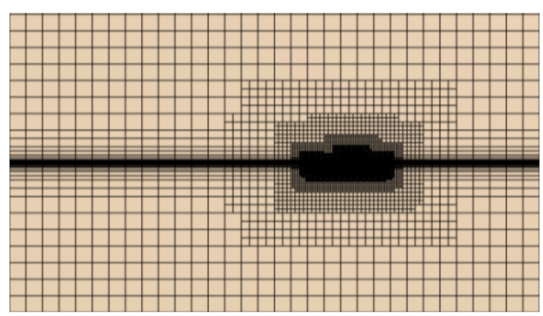

FIGURE 4. MESH DISTRIBUTION AT y= 0 CROSS SECTION.

3.3 Brash ice channel and ice floe particles

In the present study, a brash ice channel is established using the CFD-DEM coupling approach, informed by ice tank experimental data and statistical characteristics of Arctic sea ice[14]. The channel width is prescribed as three times the submarine beam. Individual ice floes are idealized as circular disc-shaped particles with a radius of R = 0.05 m and a thickness of 0.02 m. Fig. 5 illustrates the level ice and navigation channel arrangement: level ice fields are positioned on both lateral sides, while a brash ice channel of width 3*B* is situated along the centerline, where *B* represents the submarine beam. Tab. 2 presents the main parameters of the brash ice. In the CFD-DEM framework, ice floe particles are generated using an injector. Following the recommendations of Zhang et al.[4], the injector is positioned 0.15L upstream of the submarine bow, with its length matching the width of the brash ice channel.

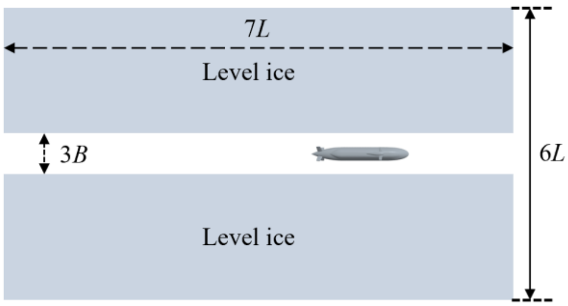

FIGURE 5. THE TOP VIEW OF LEVEL ICE AND NAVIGATION CHANNEL

TABLE 2. PRINCIPAL PARAMETERS OF BRASH ICE

Parameter	Value
Density (t/m^3)	0.916
Poisson's ratio	0.361
Young's modulus (Pa)	0.074
Drift velocity (kn)	5
Volume fraction (%)	90

4. RESULTS AND DISCUSSION

The temporal development of submarine-brash ice interaction is first presented in this section. Subsequently, parametric studies are conducted to examine the influence of submergence depth, ice floe size, and forward speed on ice loads. The summary of the simulation cases considered is provided in Tab 3.

TABLE 3. NUMERICAL SIMULATION CONDITION

	Submergence Depths *h* (m)	Ice Floe Radius *r* (m)	Speed *v* (m/s)
A	0.157/0.419/0.628	0.05	0.6
B	0.157	0.03/ 0.05 / 0.07	0.6
C	0.157	0.05	0.6/0.96/1.2

4.1 Ice load characteristics of submarines in brash ice channels

The submergence depth *h* is defined as the vertical distance from the submarine's longitudinal centerline to the undisturbed free surface. Fig. 6 presents a lateral view of the submarine operating at a submergence depth of *h* = 0.3B.

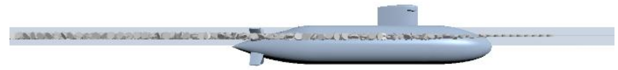

FIGURE 6. SIDE VIEW OF SUBMARINE WHILE *h*=0.3B.

To comprehensively demonstrate the submarine-brash ice interaction process, a representative case with *h*=0.3B is examined. The forward speed corresponds to 5 kn at full scale, and the simulation is conducted for a duration of 50 s. The temporal evolution of the submarine-ice interaction at selected time instants is illustrated in Fig. 7.

Fig. 7 illustrates the temporal evolution of submarine-brash ice interaction at *h* = 0.3B and 5 kn. In the initial stage, ice floes begin to contact the submarine bow with a relatively uniform distribution. As the submarine advances, the bow pushes ice floes laterally, causing them to slide along the hull surface toward the stern, forming an ice-sparse region along the channel centerline. When the interaction approaches a quasi-steady state, the ice distribution exhibits a characteristic pattern of "bow separation—lateral sliding—stern reconvergence."

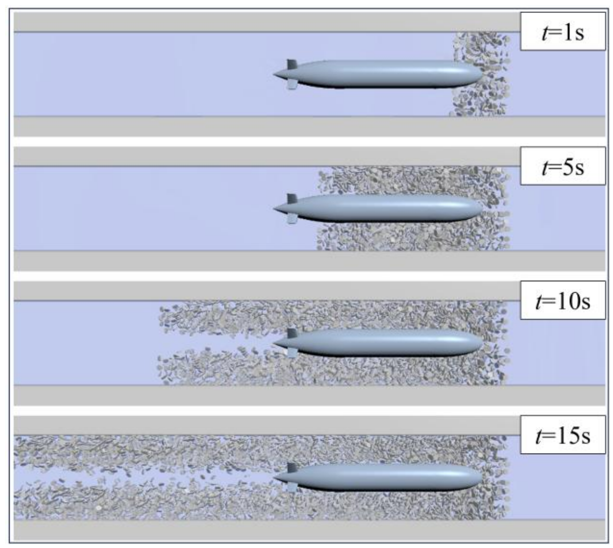

FIGURE 7. THE BOTTOM VIEW OF SUBMARINE-BRASH ICE INTERACTION PROCESS AT DIFFERENT SIMULATION TIME.

4.2 Comparison of ice loads on the submarine at varying emergence heights

To investigate the effect of submergence depth on submarine ice interaction, three submergence depths are considered: *h* = 0.3, 0.8 and 1.2B, which correspond to 0.157m, 0.419m, and 0.628m at model scale, respectively.

Fig. 8 presents the quasi-steady ice distribution at different submergence depths. At *h*=0.3B, the hull is largely exposed above the waterline, exerting a significant pushing effect on ice floes and creating a distinct ice-sparse region along the channel centerline. As the submergence depth increases to *h* = 0.8B, most of the hull is submerged with only the sail protruding above the surface, resulting in a noticeably narrower ice-sparse region. At *h*=1.2B, the submarine is fully submerged, substantially diminishing its direct interaction with the ice layer. The ice distribution becomes relatively uniform, with only minor disturbances observed directly above the sail. These results indicate that submergence depth is a critical factor governing the intensity of submarine-brash ice interaction.

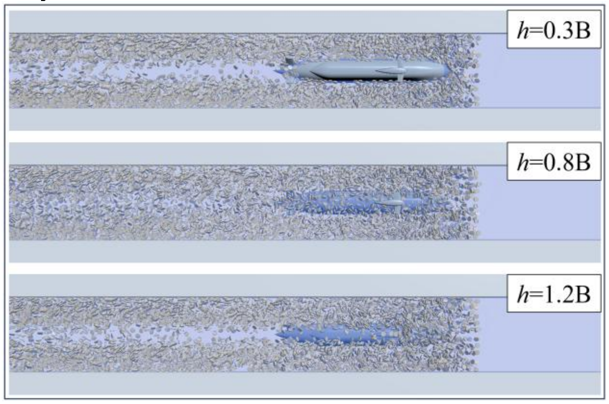

FIGURE 8. INTERACTION BETWEEN SUBMARINES AND ICE AT DIFFERENT SUBMERGENCE DEPTHS.

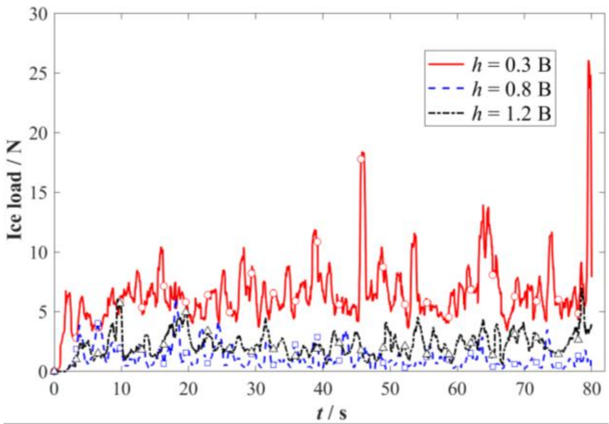

FIGURE 9. THE TIME HISTORY CURVE OF ICE LOAD ON SUBMARINE UNDER DIFFERENT SUBMERGENCE DEPTHS.

Fig. 9 presents the time histories of ice loads on the submarine at different submergence depths. All three cases exhibit pronounced load fluctuations due to intermittent collisions between ice floes and the hull. The case of *h*=0.3B shows the highest ice load magnitude, fluctuating within approximately 0-18 N with several distinct peaks. In contrast, the ice loads at *h*=0.8B and *h*=1.2B are substantially reduced, with fluctuations remaining mostly below 5N. The results indicate that shallower submergence leads to greater contact area between the submarine and ice floes, resulting in higher ice loads.

Fig. 10 presents the statistical distribution of ice loads at different submergence depths using box plots. The case of *h*= 0.3B exhibits the highest median ice load of approximately 5 N, the largest interquartile range, and extreme values reaching up to 15 N, indicating high load magnitude and significant variability. The case of *h*=0.8B shows the lowest median and variability, with the interquartile range confined to approximately 1-2 N. The ice load at *h*=1.2B is slightly higher than that at *h*=0.8B, possibly due to wave-induced disturbances from the submerged submarine affecting the ice layer above. Overall, increasing the submergence depth effectively reduces both the magnitude and variability of ice loads.

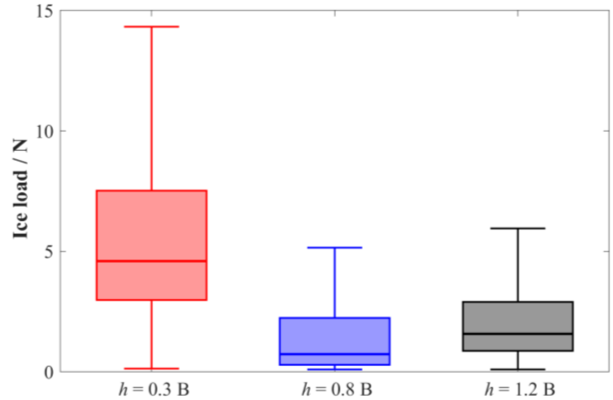

FIGURE 10. STATISTICAL DISTRIBUTION CHARACTERIS TICS OF ICE LOADS UNDER DIFFERENT SUBMERGENCE DEPTHS.

4.3 Comparison of ice loads on the submarine with varying ice floe dimensions

In order to investigate the influence of ice floe size on submarine-brash ice interaction, three ice floe radii are examined: *r* =0.6, 1.0, and 1.4R, with corresponding model-scale values of 0.03 m, 0.05 m, and 0.07 m, respectively.

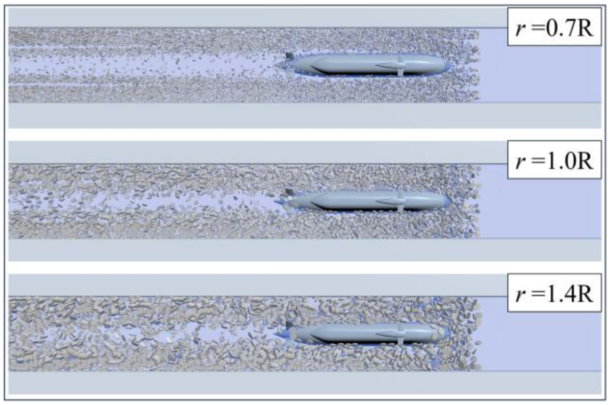

FIGURE 11. INTERACTION BETWEEN SUBMARINES AND ICE AT DIFFERENT ICE FLOE DIMENSIONS.

Fig. 11 presents the quasi-steady ice distribution at different ice floe sizes. At *r* =0.7R, the smaller ice floes are readily deflected by the hull, resulting in a wide ice-sparse region along the channel centerline. As the ice floe size increases to *r* =1.0R, the ice-sparse region narrows and ice accumulation at the bow becomes more pronounced. At *r* =1.4R, the larger ice floes possess greater inertia and are more resistant to displacement, leading to a further reduction in the ice-sparse region width and denser ice distribution around the hull, with more frequent ice-hull contact. The results indicate that larger ice floe sizes diminish the submarine's ability to clear ice from its path, consequently increasing ice loads.

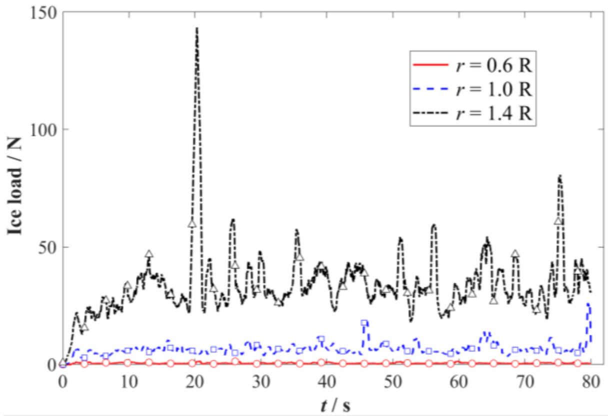

FIGURE 12. THE TIME HISTORY CURVE OF ICE LOAD ON SUBMARINE UNDER DIFFERENT ICE FLOE DIMENSIONS.

Fig. 12 presents the time histories of ice loads on the submarine under different ice floe sizes. At *r* =0.6R, ice loads are negligible as the small ice floes are unable to generate effective collisions with the hull. When the ice floe size increases to *r* = 1.0R, ice loads rise moderately, fluctuating within approximately 0-15 N. At *r* =1.4R, ice loads increase dramatically, with mean values of approximately 30-40 N and peak values reaching up to 140N, accompanied by severe fluctuations. The results demonstrate that ice floe size significantly affects ice loads, as larger ice floes possess greater mass and inertia, generating more intense impact forces upon collision.

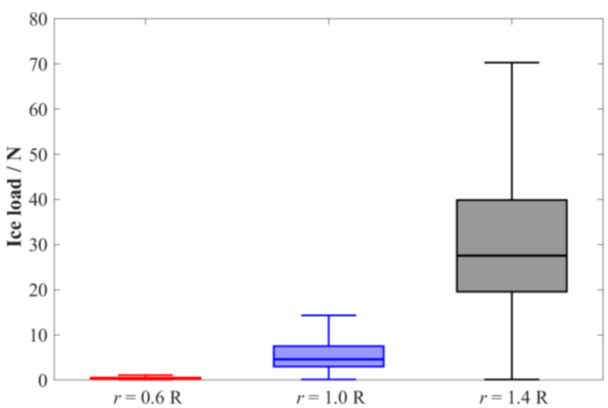

FIGURE 13. STATISTICAL DISTRIBUTION CHARACTERIS TICS OF ICE LOADS UNDER DIFFERENT ICE FLOE DIME NSIONS.

Fig. 13 presents the statistical distribution of ice loads under different ice floe sizes using box plots. At *r* = 0.6R, ice loads are minimal, with both the median and interquartile range approaching zero. At *r* =1.0R, the median ice load is approximately 5 N, with an interquartile range of 2-7 N and extreme values around 15 N. At *r* = 1.4R, ice loads increase substantially, with a median of approximately 28 N, an interquartile range of 20-40 N, and extreme values reaching up to 70 N, exhibiting the highest variability. The results indicate that increasing ice floe size not only elevates the mean ice load but also significantly increases load variability and the probability of extreme peak events.

4.4 Comparison of ice loads on the submarine at varying speed

For purpose of examining the effect of forward speed on submarine-brash ice interaction, three forward speeds corresponding to full-scale values of *v* = 5, 8, and 10 kn are considered, equivalent to 0.6 m/s, 0.96 m/s, and 0.2 m/s in the present simulations.

Fig. 14 presents the quasi-steady ice distribution at different forward speeds. At *v*=5 kn, the pushing effect of the submarine on ice floes is relatively weak, resulting in a narrow ice-sparse region along the channel centerline. As the speed increases to *v*=8 kn, the pushing and deflecting effects are enhanced, noticeably widening the ice-sparse region with more effective lateral dispersion of ice floes. At *v* =10 kn, the strong pushing effect generated at high speed further expands the ice-sparse region, leaving the channel centerline nearly ice-free, with ice floes rapidly deflected and accumulated along the channel edges. The results indicate that higher forward speeds enhance the submarine's ice-clearing capability, while simultaneously increasing collision frequency and impact intensity.

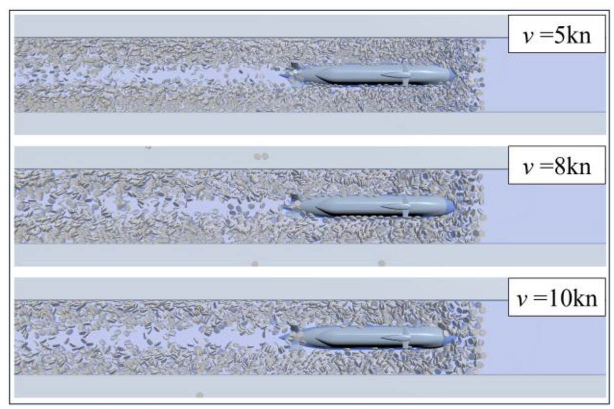

FIGURE 14. INTERACTION BETWEEN SUBMARINES AND ICE AT DIFFERENT SPEED.

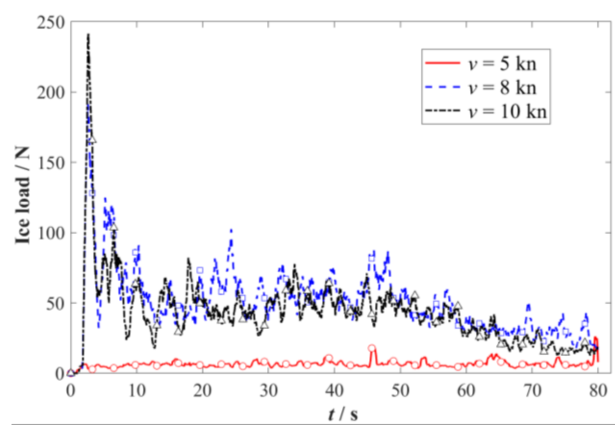

FIGURE 15. THE TIME HISTORY CURVE OF ICE LOAD ON SUBMARINE UNDER DIFFERENT SPEED.

Fig. 15 presents the time histories of ice loads on the submarine at different forward speeds. At *v* =5 kn, ice loads remain relatively low and stable, mostly below 10 N. When the speed increases to v =8 kn and v =10 kn, ice loads increase significantly. A pronounced impact peak is observed during the initial stage (t<10 s), reaching up to 240 N, followed by gradual attenuation to a relatively stable fluctuation phase with mean values of approximately 40-60 N. The ice load time histories for the two higher speeds are comparable, suggesting that beyond a certain velocity threshold, the growth rate of ice loads tends to plateau.

Fig. 16 presents the statistical distribution of ice loads at different forward speeds using box plots. At v =5 kn, ice loads are minimal, with a median of approximately 5 N, an interquartile range of 3-8 N, and extreme values around 15 N. When the speed increases to v =8 kn, ice loads rise substantially, with a median of approximately 38 N, an interquartile range of 20-65 N, and extreme values reaching up to 125 N, exhibiting the highest variability. At v=10 kn, the median ice load is approximately 30 N, slightly lower than that at v =8 kn, although extreme values still reach 110 N. The results indicate that increasing forward speed significantly elevates both the magnitude and variability of ice loads. However, beyond a certain speed threshold, the rate of increase diminishes, possibly attributed to the rapid deflection of ice floes at higher speeds, which reduces ice-hull contact duration.

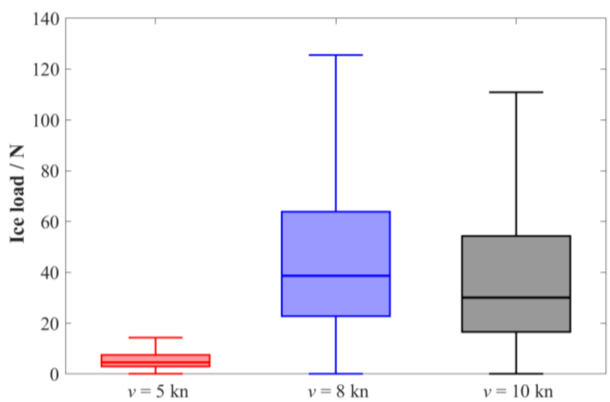

FIGURE 16. STATISTICAL DISTRIBUTION CHARACTERISTICS OF ICE LOADS UNDER DIFFERENT SPEED.

5. CONCLUSION

This study numerically investigates submarine-brash ice interaction using a CFD-DEM coupling approach, systematically analyzing the effects of submergence depth, ice floe size, and forward speed. The results demonstrate that submergence depth is a critical factor governing ice loads, with significantly higher loads observed at shallower depths. Larger ice floe sizes lead to increased ice inertia and substantially elevated ice loads with greater variability. Higher forward speeds intensify collision frequency and impact forces, although the rate of ice load increase diminishes beyond a certain velocity threshold.

ACKNOWLEDGEMENTS

This work is supported by the National Natural Science Foundation of China (Nos. 52571360 and 52131102), to which the authors are most grateful.

REFERENCES

[1] Thomson J, Ackley S, Girard-Ardhuin F,et al. Overview of the Arctic Sea State and Boundary Layer Physics Program[J]. *Journal of Geophysical Research Oceans*, 2018.

[2] Zou M, Zou Z Z, Zou L, et al.Numerical Modeling of Ship-Ice-Water Interaction for Freerunning Ships in Pack Ice[J]. *Journal of Ship Mechanics*, 2025, 29(6).

[3] Xie C, Zhou L, Wu T, et al. Resistance performance of a ship in model-scaled brash ice fields using CFD and DEM coupling model[J]. *Frontiers in Energy Research*, 2022,10.

[4] Zhang J , Zhang Y , Shang Y,et al. CFD-DEM based full-scale ship-ice interaction research under FSICR ice condition in restricted brash ice channel[J]. *Cold Regions Science and Technology*, 2022, 194:103.

[5] Huang L F, Li Z Y, Ryan C, et al. Ship resistance when operating in floating ice floes: Derivation, validation, and application of an empirical equation[J]. *Marine Structures*, 2021,79, 103057.

[6] Huang L F, Tuhkuri J, Igrec B, et al. Ship resistance when operating in floating ice floes: A combined CFD&DEM approach[J]. *Marine Structures*,2020, 74, 102817.

[7] Wang C, Hu X H, Tian T P, et al. Numerical simulation of ice loads on a ship in brash ice fields using an elastic ice model[J]. *International Journal of Naval Architecture and Ocean Engineering*, 2020, 12:414-427.

[8] Ibrahim R A , Chalhoub N G , Falzarano J .Interaction of Ships and Ocean Structures With Ice Loads and Stochastic Ocean Waves[J].*Applied Mechanics Reviews*, 2007, 60(5):246.

[9] Menter F R. Two-equation eddy-viscosity turbulence models for engineering applications[J]. *AIAA Journal*, 1994, 32.

[10] Yan Y H, Shi Y Y, Li Z F, et al. Research on ice load on submarine near to water surface in brash ice channel[J]. *Shipbuilding of China*, 2022, 63(1): 12. (in Chinese)

[11] Luo W Z, Jiang D P, Wu T C, et al. Numerical simulation of an ice-strengthened bulk carrier in brash ice channel[J]. *Ocean Engineering*, 2020,196, 106830.

[12] Joubert P N. Some aspects of submarine design part 1: hydrodynamics[R]. Defence Science and Technology, Australia, Technical Report TR-1622, 2004.

[13] Joubert P N. Some aspects of submarine design part 2: shape of a submarine 2026[R]. Defence Science and Technology, Australia, Technical Report TR-1920, 2006.

[14] Kwok R. Arctic sea ice thickness, volume, and multiyear ice coverage: Losses and coupled variability (1958–2018)[J]. *Environmental Research Letters*, 2018, 13(10), 105005.